ACS NANO

www.acsnano.org

ARTICLE

Ultrafast Carrier Drift Transport Dynamics in $CsPbI_3$ Perovskite Nanocrystalline Thin Films

Kanishka Kobbekaduwa, Exian Liu, Qian Zhao, Jasjit Singh Bains, Jianbing Zhang, Ying Shi, Haimei Zheng, Dawen Li, Tong Cai, Ou Chen, Apparao M. Rao, Matthew C. Beard, Joseph M. Luther, and Jianbo Gao*

Cite This: *ACS Nano* 2023, 17, 13997−14004

Read Online

ACCESS | Metrics & More | Article Recommendations | Supporting Information

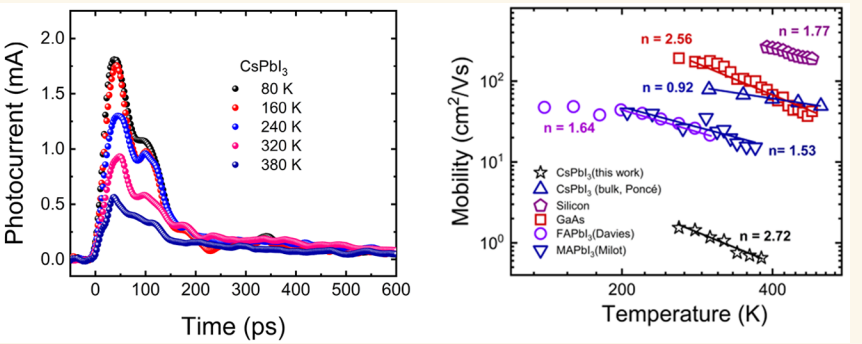

ABSTRACT: **We study the early time carrier drift dynamics in $CsPbI_3$ nanocrystal thin films with a sub 25 ps time resolution. Prior to trapping, carriers exhibit band-like transport characteristics, which is similar to those of traditional semiconductor solar absorbers including Si and GaAs due to optical phonon and carrier scattering at high temperatures. In contrast to the popular polaron scattering mechanism, the $CsPbI_3$ nanocrystal thin film demonstrates the strongest optical phonon scattering mechanism among other inorganic−organic hybrid perovskites, Si, and GaAs. This ultrafast dynamics study establishes a foundation for understanding the fundamental carrier drift properties that drive perovskite nanocrystal optoelectronics.**

KEYWORDS: *phonons, polarons, mobility, photocurrent, scattering*

INTRODUCTION

It remains a challenge to identify the drift dynamics of carrier transport in the ultrafast temporal region (early time) of optoelectronic materials and devices. However, the understanding of carrier drift dynamics in early time is important as it influences the subsequent dynamics such as carrier scattering, recombination, and trapping, which are the foundations of device efficiency and performance. For decades, the research community has relied on the traditional time-resolved optical spectroscopic techniques including pump−probe and fluorescence approaches to investigate ultrafast dynamics, but they are limited to carrier diffusion dynamics. Particularly, this is urgent for emergent nanostructured organic/inorganic perovskite nanocrystals (NCs) such as cesium lead halide ($CsPbX_3$, X = Cl, Br, I) and methylammonium (MA) or formamidinium (FA) lead halide, which are typically solution-processed at low temperatures and demonstrate superior device performance in optoelectronic applications such as solar cells,[1] X-ray detectors,[2] light-emitting diodes (LEDs),[3] etc. However, due to the low-dimensional nanostructure and low-temperature processing, researchers have to deal with large defect densities, which prevent the evaluation of critical phonon scattering mechanisms. Thus, there is an open question in the field of nanocrystals in terms of carrier transport properties on whether these solution-processed nanostructured semiconductors are either similar to or different from their counterpart, crystalline semiconductors, particularly when used as solar cell absorbers.

In this work, we address this open question using ultrafast photocurrent spectroscopy (UPCS) by investigating the carrier drift dynamics in perovskite NC thin films and traditional solar cell absorbers such as silicon (Si) and GaAs. In contrast to

Received: May 4, 2023
Accepted: July 7, 2023
Published: July 14, 2023

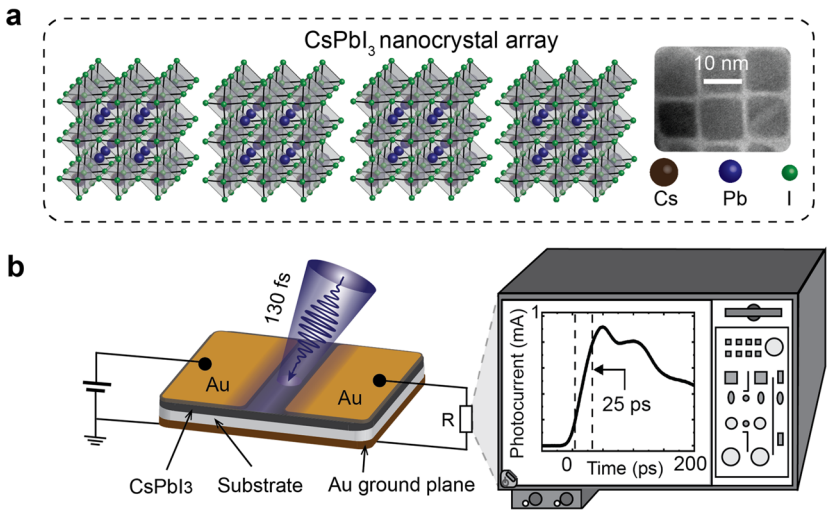

Figure 1. Schematic of the UPCS. (a) Lattice structure and transmission electron microscopy (TEM) image of a $CsPbI_3$ NC array (scale bar ~10 nm). (b) UPCS with sub 25 ps time resolution comprised of a coplanar transmission line as a high-speed photocurrent waveguide and a NC thin film that is illuminated by an ultrafast laser pulse to generate photocurrent that is collected by a sampling oscilloscope. The laser beam covers the entire device including the NC film and a section of the Au electrodes.

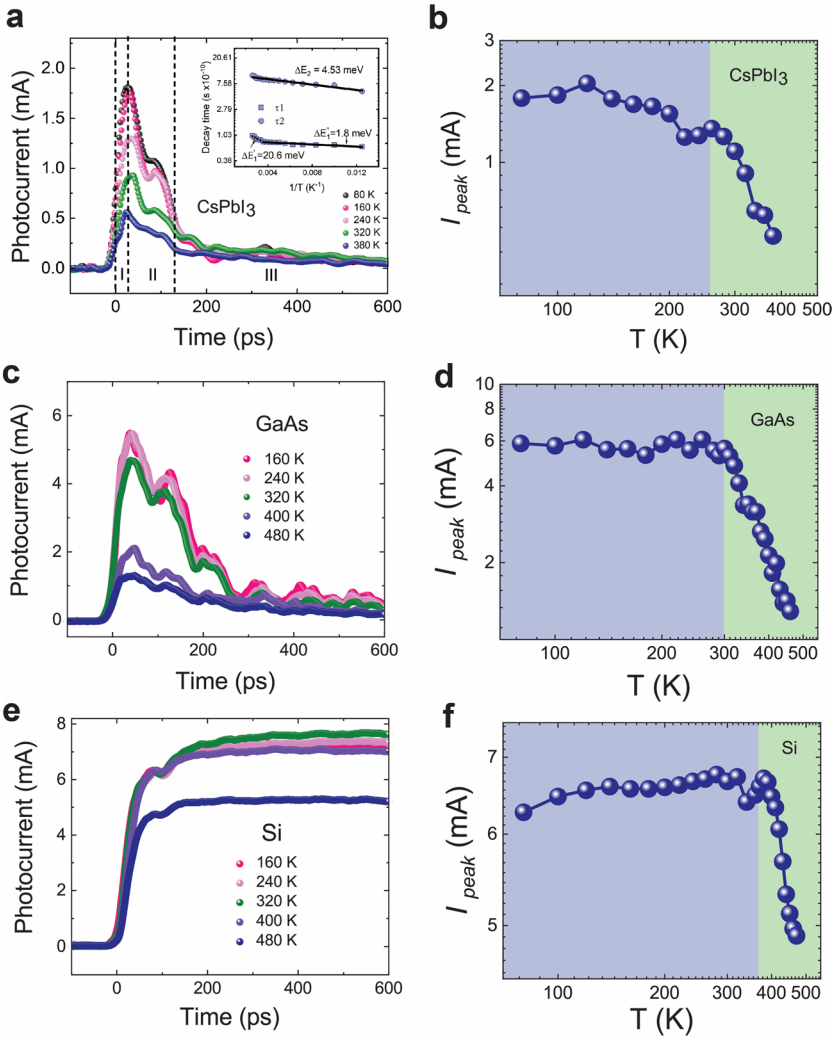

Figure 2. Ultrafast photocurrent dependence on temperature. (a, c, e) Temperature-dependent ultrafast photocurrents for $CsPbI_3$ NC films, doped GaAs, and lightly doped Si, respectively. The corresponding temperature-dependent photocurrent peak on a log−log scale is shown in (b), (d), and (f). The inset of (a) shows the Arrhenius plot for photocurrent decay.

https://doi.org/10.1021/acsnano.3c03989
ACS Nano 2023, 17, 13997−14004

traditional Carrier drift dynamics is generally found through traditional time-resolved laser spectroscopies, which include (i) time-resolved photoluminescence (TRPL)[4] and (ii) pump−probe techniques such as transient absorption,[5] terahertz-time domain spectroscopy (THz-TDS),[6−9] and many others,[10−12] the fundamental underlying disadvantage of these techniques is that the focus is limited to the carrier diffusion dynamics, where carriers are confined in nanometer short-range diffusion behavior. In contrast, UPCS investigates carrier drift dynamics, where carriers can conduct a range of transports in a couple hundred nanometers. As a result, we characterize the figure of merit of carrier drift property including carrier mobility, lifetime, and defect property with a sub 25 ps time resolution. However, a TA or THz pump−probe may stand out due to their subpicosecond time resolution. Although time-resolved photoconductivity techniques such as the time-of-flight photocurrent (TOF)[13] and photo-CELIV (charge extraction by linearly increasing voltage) can characterize those critical drift parameters in photoconductive devices,[14] they are limited to defect property characterization since the time resolution is approximately tens of nanoseconds (ns),[15] which is much longer than the trapping events in most solution-processed perovskites.

Our aims are 2-fold: (1) investigate the carrier drift dynamics prior to carrier trapping events and (2) identify the carrier scattering mechanism in perovskite NCs and compare it with well-known semiconductor solar absorbers including Si and GaAs. To this end, an inorganic $CsPbI_3$ NC array is used as a model system. The lattice structure as well as SEM images of perovskite NCs are shown in Figure 1a. Unlike bulk perovskites, these have wider tunability in terms of NC size, structure (quantum dots, layered materials, and nanotube), surface chemistry, and composition. In the ultrafast temporal region of sub 25 ps, carriers in $CsPbI_3$ demonstrate band-like transport due to interactions with optical phonons that dominate in a higher temperature regime (HT) (>240 K), In the lower temperature regime (LT) (<240 K), defect scattering balances out the electron−phonon scattering dominated by low-energy acoustic phonons. As determined through the mapping of a temperature (transport) index, the $CsPbI_3$ NC thin films exhibited the strongest optical phonon interaction compared to other inorganic−organic hybrid perovskites, Si, and GaAs. Thus, optical phonon scattering is the dominant scattering mechanism in contrast to the popular polaron carrier interaction.

RESULTS AND DISCUSSION

As shown in Figure 1b, by integrating a $CsPbI_3$ NC thin-film photoconductor into a transmission line architecture as a high-speed photocurrent waveguide, the carrier drift dynamics can be investigated in photoconductors *in operando* with a sub 25 ps time resolution by UPCS.[16−18] A detailed NC film morphology and experimental configuration can be found in Supplementary Methods and Figure S1. To facilitate carrier transport and enable wave function coupling among nanocrystals, the NCs are treated with MeOAc (methyl acetate) and the long-chain ligands are replaced with short-chain acetate ligands. Figure 2a shows the various temperature-dependent photocurrent decays for the $CsPbI_3$ NC film. The photocurrent is proportional to the photogenerated charge carrier density, as the majority of the photogenerated charge carriers are extracted as photocurrent. A typical photocurrent can be characterized by a fast rise to ∼25 ps followed by a rapid decay up to 125 ps and then a slow tail extending beyond 600 ps (zero time is at 10% of the peak photocurrent). These three temporal regions are denoted by dashed vertical lines in Figure 2a. In the first temporal region I, during the initial rise to ∼25 ps, the peak photocurrent (I_{peak}) decreases with increasing temperature from 240 to 400 K, as shown in Figure 2b, and can be described by

$$I_{peak} \approx T^{-n} \tag{1}$$

where n is an index (temperature or transport index) and T is the temperature. This classic power-law relation is the signature of band-like transport due to carrier−phonon scattering. To highlight the phonon scattering mechanism, rather than the defect scattering, here we adopt the classic and general band-like term in semiconductors.

In region II, two competing transport mechanisms govern the photocurrent response between ∼25 and ∼125 ps. On one hand, the photocurrent dependence continues to decrease with increasing temperature, indicating the presence of phonon scattering. On the other hand, the time decay (Figure S3) shows an opposite trend; it increases with increasing temperature, which is a signature of hopping transport due to defect scattering. An Arrhenius relation for decay time with temperature can be written as

$$\tau \approx e^{-\Delta E/k_B T} \tag{2}$$

where ΔE is the activation energy or defect energy level in this case, k_B is the Boltzmann constant, and τ is the decay time constant. The thermal activation energy of ∼1.8 meV is derived as described in a Supplementary Note. Transport dynamics post 25 ps are shown in the inset of Figure 2a. In region III, i.e., beyond ∼125 ps, the slow decay tail can be attributed to a hopping transport mechanism with an activation energy of ∼4.5 meV. As reported by our previous work,[18] the increasing thermal activation with time indicates that carriers follow a multiple trapping and release transport mechanism. Figure S2 depicts a complete photocurrent decay with an average carrier lifetime in the temperature range from 80 to 400 K (see Table S1). Thus, we can conclude that in the early time prior to 25 ps, the carrier transport is dominated by the carrier−phonon scattering mechanism, rather than the trapping or defect scattering mechanism.

To highlight the significance of drift dynamics before trapping (based on our data, we consider initial trapping occurs in region I as depicted in Figure 2a), we compare the ultrafast photocurrents of $CsPbI_3$ NC films, with the traditional semiconductor solar absorbers under the same electrical field and the photon density in the range of 10^{16} cm^{-3} (Figures 2c,e). For doped GaAs with a defect density >10^{15} cm^{-3}, the temperature-dependent photocurrent decay trend is similar to that of the $CsPbI_3$ NC films, i.e., a fast rise followed by a rapid decay. Similarly, the photocurrent peak decreases with increasing temperature in the range from 300 to 500 K, as illustrated in Figure 2d, which can be attributed to carrier−phonon scattering. Moreover, the decay constant also increases because of defect scattering. In contrast, the photocurrent exhibits a fast rise for n-type Si with a defect density <10^{15} cm^{-3}, followed by a plateau up to a couple of nanoseconds, as shown in Figure 2e. This is mainly due to the low defect density, which primarily lowers the rate of carrier recombination (trap-assisted recombination) and increases the carrier lifetime. In contrast, materials with defects such as GaAs and $CsPbI_3$ show a sharp decay in photocurrent as excited carriers

https://doi.org/10.1021/acsnano.3c03989
ACS Nano 2023, 17, 13997−14004

recombine within defect states, thus reducing the carrier lifetime. Similar to the $CsPbI_3$ NC films and GaAs, the photocurrent peak is attributed to optical phonon scattering, since its amplitude decreases with increasing temperature (from 400 to 500 K), as illustrated in Figure 2f. In addition to the temporal evolution of the photocurrent, as seen in Figure 2a,c,e, the evolution of the peak photocurrent with temperature (Figure 2b,d,f) also indicates the carrier transport mechanism. All three semiconductors exhibit a similar transition of the transport mechanism in the low- and high-temperature regimes. The transition temperatures are 300 and 380 K for doped GaAs and slightly doped Si, respectively. For GaAs, below 300 K this is due to the combination of defect scattering and phonon scattering mechanisms, which demonstrate an opposite temperature dependence. As a result, the photocurrent peak remains constant. For Si, the defect scattering mechanism dominates below 380 K and the photocurrent decreases with decreasing temperature. For the $CsPbI_3$ NC film and below 240 K, we note that the photocurrent peak of $CsPbI_3$ NC films exhibits a weak temperature dependence. We attribute this weak temperature dependence to a change in scattering mechanism, from piezoelectric scattering due to acoustic phonons and space-charge scattering due to impurities at low temperatures, to optical phonon scattering at higher temperatures based on previous work.[19]

The sum of the mobility, which is a critical parameter to evaluate the carrier transport property, can be derived from the peak photocurrent as described[20]

$$I_{peak} = e\eta(\mu_h + \mu_e)\frac{NE}{L} \quad (3)$$

where μ_h and μ_e are the hole and electron mobilities, respectively, $\mu = \mu_h + \mu_e$ is the total carrier mobility, e is the electron charge, η is the quantum yield which is the product of quantum efficiency of carrier photogeneration and carrier collection, N is the effective photon number, E is the electric field, and L is the electrode spacing. For $CsPbI_3$ NC thin films, the calculated sum of the carrier mobility at room temperature is ~2.5 $cm^2/(V\ s)$. (here we assume the quantum yield η is 100%)[21] (see Supplementary Note, carrier mobility calculations, and Figure S4 for calculations). Similarly, for GaAs and doped Si, the calculated carrier mobilities at room temperature are ~303 and ~177 $cm^2/(V\ s)$, respectively. We note that these values are lower than previously reported mobility values for GaAs and Si with comparable dopant concentrations and defect densities. For instance, the electron mobility is ~3000 $cm^2/(V\ s)$ for GaAs[22] and ~1500 $cm^2/(V\ s)$ for Si.[23] The calculated carrier mobilities are lower due to the assumed high quantum yield value of 100%. It is worth noting that, assuming 10% quantum yield, the mobility increases from 2.5 $cm^2/(V\ s)$ to ~25 $cm^2/(V\ s)$, and it is in the same range as that characterized by the THz TDS.[8] Moreover, this high mobility value (>2.5 $cm^2/(V\ s)$) at room temperature is consistent with the phonon scattering mechanism in $CsPbI_3$ films, which is a signature of band-like transport. The linear dependence on electric field and laser intensity at 80 K for $CsPbI_3$ NC thin films (Figures S5–S7), as well as for GaAs and Si (Figure S8), suggests that all three semiconductors exhibit the same photogeneration mechanism resulting from the free carrier generation. At room temperature, from the sub ps to sub 25 ps region, the calculated minimum drift length of the carriers under a moderate electrical field of 2×10^4 V/cm with minimum mobility of ~2.5 $cm^2/(V\ s)$ is ~12 nm, which is equivalent to around more than one NC width, well beyond the couple nanometer diffusion length previously reported using ultrafast optical spectroscopy.[24]

Because the hopping transport mechanism has been well studied through the carrier trapping model in perovskite bulk films[18,25,26] and NCs,[27,28] here, we highlight the pretrapping dynamics to gain insights into the carrier–phonon interactions. Indeed, the early-time phonon scattering in $CsPbI_3$ has been reported by Wong and Bonn et al. using transient absorption and THz pump–probe approaches, respectively.[8,29] The strength of the carrier–phonon interaction is related to the temperature-dependent carrier mobility μ as

$$\mu \approx T^{-n} \quad (4)$$

The n value is a "normalization" parameter despite the fact that different measurement techniques have different mobility characterization systematic errors. Also, the n value is an indication of various phonon modes. For instance, the stronger the phonon–carrier interaction, the larger the n value. In classic crystalline semiconductors, the n value of 1.5 is an indication of an acoustic phonon, and larger than 1.5 is an indication of an optical phonon.[30] However, the n index value is also dependent on nanostructure, temperature, etc. as discussed in the following section. As shown in Figure 3, for

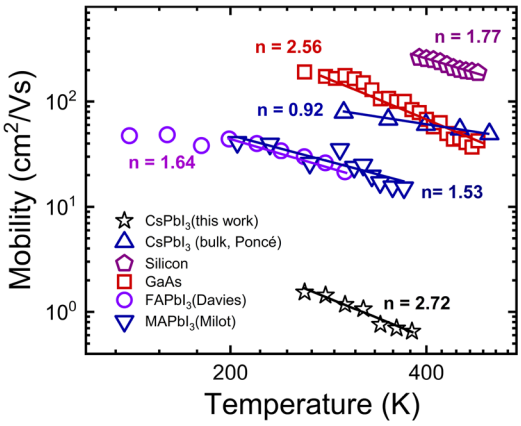

Figure 3. Carrier mobility dependence on temperature. Carrier mobility dependence on temperature in two types of semiconductors: a typical crystalline polar semiconductor such as GaAs and Si and bulk $CsPbI_3$ (Ponce) and solution-processed $MAPbI_3$ (Milot), $FAPbI_3$ (Davies), and $CsPbI_3$ NC perovskites.

$CsPbI_3$ NCs, in the temperature range of 240 to 380 K, the n value is ~2.7 in contrast to the same bulk material (n = 0.92).[31] While at low temperatures (<240 K), it decreases to n = 0.1, which we attribute to a combination of defect scattering and acoustic phonon scattering (see Figure S9). In contrast, the high-temperature n value of the $CsPbI_3$ NC is larger in comparison to that of (1) traditional semiconductor solar absorbers, n = 1.77 and n = 2.56 for Si and GaAs, respectively, and (2) low-temperature solution-processed organic lead halide perovskites such as $MAPbI_3$ (n = 1.53)[32] and $FAPbI_3$ (n = 1.64).[33] Particularly, for $MAPbI_3$ and $FAPbI_3$, there is a phase transition from an orthorhombic to a tetragonal phase at approximately 150 K. Therefore, we extract the n value above the phase transition temperature.[34] Although the mobility dependence on temperature of those semiconductor materials has been characterized by various techniques,[35] the "normal-

https://doi.org/10.1021/acsnano.3c03989
ACS Nano 2023, 17, 13997–14004

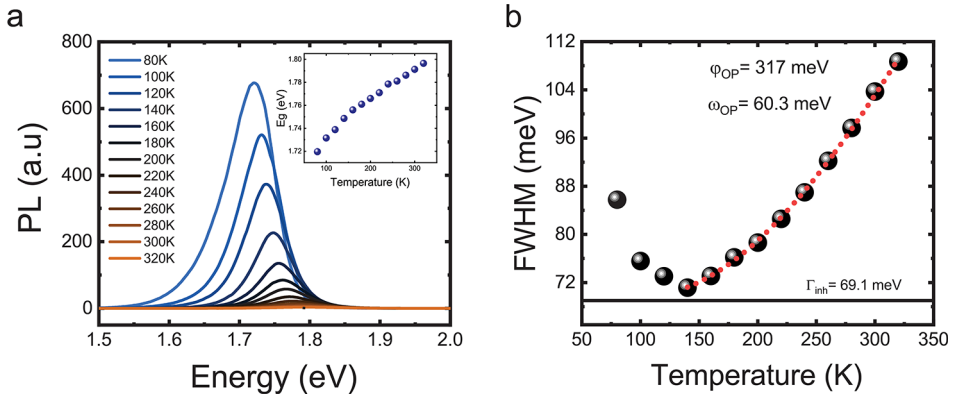

Figure 4. Steady-state PL emission. (a) PL emission spectrum of $CsPbI_3$ NCs from 80 to 320 K. There is a clear blue shift and decrease in PL intensity in the spectrum with increasing temperature, and the inset shows the change in the peak which corresponds to lowering of the band gap. (b) The corresponding full width at half-maximum (fwhm) Γ values. The dotted line is a fitting corresponding to $\Gamma(T) = \Gamma_{inh} + \frac{\varphi_{OP}}{e^{(E_{op}/k_BT)} - 1}$, where the second term represents optical phonon scattering.

ized" n index value is weakly dependent on characterization approaches.

In the perovskite community, the origin of carrier scattering mechanisms is under debate.[36] First, we exclude the acoustic phonon scattering mechanism. This is because the n = 1.5 temperature dependence is generally expected due to acoustic phonon scattering, although the converse may not necessarily hold. We also exclude the popular polaron scattering mechanism. A polaron is a cloud of phonon modes, and due to the large organic molecules, such as MA and FA, it is plausible that MA or FA molecules distort the lattice structure along with the phonon modes. As a result, this will reduce the interaction among the phonon interaction with carrier, leading to smaller n index value, as reported by Motta and Sanvito in $CsPbBr_3$,[37] which mainly resulted from the polaron scattering mechanism, while the polaron prohibits carrier transport. Furthermore, first-principles calculation without assumption of the temperature dependence shows a smaller n index value.[38] Here, the larger n index value in $CsPbBr_3$ indicates that the optical phonon−carrier interaction is the dominant mechanism. Below we focus on the underlying mechanism for the varying n values in the high-temperature regime and their relationship to the carrier−optical phonon scattering process.

In solution-processed perovskites, the carrier−phonon coupling is aligned with the bond characteristics of the halide anion (in this case, I^-) and the central organic (MA^+, FA^+) or inorganic (Cs^+) cation. The carrier−phonon coupling constant is determined by the bond length d of the cation (A)−halogen (X) bond (MA-I, FA-I, Cs-I) and the coordination number a defining the number of bonds that connect X to A, both of which are large ($d \approx 4.5$ Å; a = 12), leading to strong theoretical optical phonon coupling in $CsPbI_3$. In comparison to MA or $FAPbI_3$, which have $d \approx 2.75$ Å and a = 3,[39] both d and a values are large for $CsPbI_3$, as depicted in Figure S10 and the Supplementary Note (carrier−phonon coupling). Although carrier−phonon interactions can also be enhanced in NCs due to quantum confinement,[40] the $CsPbI_3$ NCs in this work are much larger (12 nm). Thus, the effect of quantum confinement on the phonon interactions is negligible. Unlike $CsPbI_3$, both GaAs and Si are single crystalline, and the strong carrier−phonon coupling (as seen in the large n values shown in Figure 3) is mainly due to structural symmetry.

To quantify the relationship between the above phonon coupling mode and the n values, we turn to the following equations defined by Fivaz and Mooser[41] to gauge the type of optical phonon involved in the scattering process

$$n = \frac{\left(\frac{\hbar\omega}{k_BT}\right)e^{\hbar\omega/k_BT}}{e^{\hbar\omega/k_BT} - 1} - 1 \quad (5)$$

where $\hbar$ is the reduced Planck's constant and ω is the optical frequency, respectively. Using an n value of 2.7 for the photocurrent peak (from Figure 3) in eq 5, we obtain $E_{op} = \hbar\omega \approx 64$ meV at 300 K and an average energy of ~62 meV (in the range of 20−100 ps) at 300 K (Figure S11). In comparison, the derived optical phonon energy is ~66 meV for Si and ~85 meV for GaAs, respectively, and these values are consistent with previous reports.[42,43]

To validate the optical phonon mode generated, we use temperature-dependent steady-state photoluminescence (PL) as shown in Figure 4a. A similar approach such as Raman spectroscopy can be used; the temperature-dependent photoluminescence stands out due to its signal to noise ratio. The full width at half-maximum (fwhm) can be described as $\Gamma(T) = \Gamma_{inh} + \frac{\varphi_{OP}}{e^{(E_{op}/k_BT)} - 1}$ (Figure 4b), where Γ_{inh} is a temperature-independent inhomogeneous constant arising from scattering due to crystalline imperfections and exciton−exciton interactions,[44] φ_{OP} is the amplitude, and E_{op} is the optical phonon. From our analysis, we obtain a phonon energy $E_{op} \approx 60$ meV. Thus, the energy of the optical phonons is similar to the steady-state phonon energy calculated from Figure 4b. The value extracted above for phonon energy E_{op} is far larger than what was observed in $CsPbI_3$.[45,46] Most likely, the extra energy is attributed to high-energy phonon modes from the surface ligands.

CONCLUSIONS

By elucidating the nature of carrier drift dynamics and carrier scattering mechanisms, particularly in the ultrafast temporal region, we highlight the optical phonon scattering mechanism similarity of $CsPbI_3$ NC films with those of traditional solar absorbers. In contrast to the popular polaron−carrier scattering, the $CsPbI_3$ NC film demonstrates the strongest optical phonon and carrier interaction among other inorganic−organic hybrid perovskites and traditional solar absorbers. Our study has profound implications for emergent organic/inorganic perovskite photonic, optoelectronic, and electronic

https://doi.org/10.1021/acsnano.3c03989
ACS Nano 2023, 17, 13997−14004

devices because we establish a foundation for describing the intrinsic electrical transport properties.

EXPERIMENTAL SECTION

Materials. Methyl acetate (MeOAc; anhydrous, 99.5%), oleic acid (OA; technical grade, 90%), cesium carbonate (Cs_2CO_3; 99.9%), octane (anhydrous, ≥99%), oleylamine (OAm; technical grade, 70%), 1-octadecene (ODE; technical grade, 90%), hexane (reagent grade, ≥95%), lead nitrate ($Pb(NO_3)_2$; 99.999%), ethyl acetate (EtOAc; anhydrous, 99.8%), and formamidinium iodide (FAI; ≥98%) were purchased from Sigma-Aldrich. Lead(II) iodide (PbI_2; 99.9985%) was obtained from Alfa Aesar.

$CsPbI_3$ NC Synthesis and Purification. The synthesis process follows a method reported by Hazarika et al.[1] with slight modification. First, to synthesize the Cs-oleate precursor, 0.407 g of Cs_2CO_3 and 1.25 mL of OA were added to 20 mL of ODE. Then the mixture was degassed at 150 °C for 20 min under a vacuum. The fully dissolved Cs-oleate precursor was kept at 150 °C under a N_2 atmosphere until needed. Subsequently, 0.5 g of PbI_2 was added to 25 mL of ODE and heated at 120 °C for 10 min under vacuum. A solution of 2.5 mL of OA was mixed with 2.5 mL of OAm (heated at 130 °C) and was then injected into the PbI_2 solution. The reaction flask was kept at 120 °C until PbI_2 was fully dissolved. Afterward, the solution was heated to 180 °C under flowing N_2. Once the solution reached 180 °C, 2 mL of the Cs-oleate precursor was immediately injected into the reaction flask, and the mixture was quenched in an ice bath. The resulting colloidal solution was left to cool to 20 °C and then mixed with 70−80 mL of MeOAc before centrifuging at 7500 rpm for 5 min. Then the precipitated $CsPbI_3$ NCs were dispersed in 5 mL of hexane, reprecipitated by adding ∼5 mL of MeOAc, and centrifuged again at 7500 rpm for 5 min. The obtained precipitate was then redispersed in 15 mL of hexane and stored in a refrigerator at 4 °C. This $CsPbI_3$ NC solution was centrifuged again at 7500 rpm for 5 min after 24 h post storage in the refrigerator to remove excess Cs-oleate and Pb-oleate. The supernatant was filtered through a 0.45 μm nylon filter before use. The synthesized NCs can be seen in Figure S1a,b.

Ligand Exchange. This synthesis procedure replaces the traditional long-chain oleate ligand from oleic acid (2.5 nm) with short-chain OAc ions by way of MeOAc. The oleate ligand consists of an 18-carbon chain; thus, the ligand exchange procedure reduces to a two-carbon chain, with the OAc ligand being ∼0.28 nm. Thus, the average distance between the two NCs is ∼0.6 nm.

Fabrication of NC Films. The $CsPbI_3$ NC films were deposited according to the method by Zhao et al.[1] with slight modifications and within a humidity-controlled box (relative humidity, ∼20−25%). First, the $CsPbI_3$ NC was prepared according to the wet synthesis method above. The films were deposited on a 10 mm × 10 mm quartz substrate. Each layer of $CsPbI_3$ QD was deposited by spin-coating at 1000 rpm for 20 s and then 2000 rpm for 5 s. Subsequently, the film was dipped into a solution of $Pb(NO_3)_2$ saturated in MeOAc and then rinsed in a pure MeOAc solution. A thin film with ∼250 nm thickness was produced by repeating the process of spin-coating QDs and soaking them in the solution three times. Finally, the film was soaked in FAI-saturated EtOAc solution for 10 s and rinsed in the neat MeOAc solution. The cross-section of the films is shown in the TEM images (Figure S1c,d) captured via an FEI Tecnai F20 electron microscope with 200 kV accelerating voltage.

ASSOCIATED CONTENT

Data Availability Statement

All data are available in the main text or Supporting Information.

Supporting Information

The Supporting Information includes The Supporting Information is available free of charge at https://pubs.acs.org/doi/10.1021/acsnano.3c03989.

Detailed experimental setup engineering design, carrier transport property value calculations including mobility, lifetime, drift length, and quantum efficiency, photocurrent dependence on temperature, electrical field, and laser intensity of Si, GaAs, and $CsPbI_3$ (PDF)

AUTHOR INFORMATION

Corresponding Author

Jianbo Gao − *Department of Chemistry, Yousef Haj-Ahmad Department of Engineering, Brock University, St Catharines, Ontario L2S 3A1, Canada;* orcid.org/0000-0001-6203-5338; Email: jianbogao.nano@gmail.com

Authors

Kanishka Kobbekaduwa − *Department of Physics and Astronomy, Clemson University, Clemson, South Carolina 29634, United States;* orcid.org/0000-0002-3414-741X

Exian Liu − *Department of Physics and Astronomy, Clemson University, Clemson, South Carolina 29634, United States*

Qian Zhao − *Chemistry & Nanoscience Center, National Renewable Energy Laboratory, Golden, Colorado 80401, United States; School of Materials Science and Engineering, Nankai University, Tianjin 300350, People's Republic of China;* orcid.org/0000-0001-6939-3568

Jasjit Singh Bains − *Department of Chemistry, Yousef Haj-Ahmad Department of Engineering, Brock University, St Catharines, Ontario L2S 3A1, Canada*

Jianbing Zhang − *School of Optical and Electronic Information, Huazhong University of Science and Technology, Wuhan 430074, People's Republic of China;* orcid.org/0000-0003-0642-3939

Ying Shi − *Institute of Atomic and Molecular Physics, Jilin Provincial Key Laboratory of Applied Atomic and Molecular Spectroscopy, Jilin University, Changchun 130012, People's Republic of China;* orcid.org/0000-0002-6240-8795

Haimei Zheng − *Materials Sciences Division, Lawrence Berkeley National Laboratory, Berkeley, California 94720, United States;* orcid.org/0000-0003-3813-4170

Dawen Li − *Department of Electrical and Computer Engineering, Center for Materials for Information Technology, The University of Alabama, Tuscaloosa, Alabama 35487, United States;* orcid.org/0000-0001-8991-5431

Tong Cai − *Department of Chemistry, Brown University, Providence, Rhode Island 02912, United States*

Ou Chen − *Department of Chemistry, Brown University, Providence, Rhode Island 02912, United States;* orcid.org/0000-0003-0551-090X

Apparao M. Rao − *Department of Physics and Astronomy, Clemson University, Clemson, South Carolina 29634, United States;* orcid.org/0000-0002-1450-3499

Matthew C. Beard − *Chemistry & Nanoscience Center, National Renewable Energy Laboratory, Golden, Colorado 80401, United States;* orcid.org/0000-0002-2711-1355

Joseph M. Luther − *Chemistry & Nanoscience Center, National Renewable Energy Laboratory, Golden, Colorado 80401, United States;* orcid.org/0000-0002-4054-8244

Complete contact information is available at: https://pubs.acs.org/10.1021/acsnano.3c03989

https://doi.org/10.1021/acsnano.3c03989
ACS Nano 2023, 17, 13997−14004

Author Contributions

K.K., E.L., and Q.Z. performed the experiments. K.K., E.L., and Q.Z. contributed equally to this work. J.S.B., J.Z., Y.S., H.Z., D.L., T.C., O.C., A.M.R., M.C.B., and J.M.L. were involved in the technical discussion. J.G. supervised and designed the project. All authors discussed the results and commented on the manuscript.

Notes

This manuscript was previously uploaded to a preprint server, and we have accessed the preprint on July 06, 2023. Kanishka Kobbekaduwa, Exian Liu, Qian Zhao, Pan Adhikari, Chendi Xie, Jianbing Zhang, Ying Shi, Haimei Zheng, Dawen Li, Hugo Sanabria, Ming Hu, Tong Cai, Ou Chen, Apparao M. Rao, Matthew C. Beard, Joseph M. Luther, and Jianbo Gao. Are solution processed CsPbI3 perovskite nanocrystalline films similar to traditional crystalline semiconductors? 2021, Research Square, URL: 10.21203/rs.3.rs-912920/v1
The authors declare no competing financial interest.

ACKNOWLEDGMENTS

We thank Russell Reynolds, Barrett Barker, and Michael Denz at Clemson University for their instrumental support. Q.Z. acknowledges National Natural Science Foundation of China (52102266) and the China Postdoctoral Science Foundation (2020M680861). M.C.B. and J.M.L. acknowledge the Center for Hybrid Organic Inorganic Semiconductors for Energy (CHOISE), an Energy Frontier Research Center funded by the Office of Basic Energy Sciences, Office of Science within the U.S. Department of Energy. Part of this work was authored by Alliance for Sustainable Energy, LLC, the manager, and operator of the National Renewable Energy Laboratory for the U.S. Department of Energy (DOE) under contract no. DE-AC36-08GO28308. The views expressed in the article do not necessarily represent the views of the DOE or the U.S. Government.

REFERENCES

(1) Zhao, Q.; Han, R.; Marshall, A. R.; Wang, S.; Wieliczka, B. M.; Ni, J.; Zhang, J. J.; Yuan, J. Y.; Luther, J. M.; Hazarika, A. Colloidal Quantum Dot Solar Cells: Progressive Deposition Techniques and Future Prospects on Large-Area Fabrication. *Adv. Mater.* **2022**, *34* (17), 2107888.
(2) Chen, Q.; Wu, J.; Ou, X.; Huang, B.; Almutlaq, J.; Zhumekenov, A. A.; Guan, X.; Han, S.; Liang, L.; Yi, Z. All-inorganic perovskite nanocrystal scintillators. *Nature* **2018**, *561* (7721), 88−93.
(3) Pacchioni, G. Highly efficient perovskite LEDs. *Nature Reviews Materials* **2021**, *6* (2), 108−108.
(4) Jia, Y.; Kerner, R. A.; Grede, A. J.; Rand, B. P.; Giebink, N. C. Continuous-wave lasing in an organic−inorganic lead halide perovskite semiconductor. *Nat. Photonics* **2017**, *11* (12), 784−788.
(5) Yang, Y.; Ostrowski, D. P.; France, R. M.; Zhu, K.; van de Lagemaat, J.; Luther, J. M.; Beard, M. C. Observation of a hot-phonon bottleneck in lead-iodide perovskites. *Nat. Photonics* **2016**, *10* (1), 53−59.
(6) Kumar, A.; Solanki, A.; Manjappa, M.; Ramesh, S.; Srivastava, Y. K.; Agarwal, P.; Sum, T. C.; Singh, R. Excitons in 2D perovskites for ultrafast terahertz photonic devices. *Sci. Adv.* **2020**, *6* (8), 1.
(7) Lan, Y.; Dringoli, B. J.; Valverde-Chavez, D. A.; Ponseca, C. S.; Sutton, M.; He, Y. H.; Kanatzidis, M. G.; Cooke, D. G. Ultrafast correlated charge and lattice motion in a hybrid metal halide perovskite. *Sci. Adv.* **2019**, *5* (5), 1.
(8) Zhang, H.; Debroye, E.; Steele, J. A.; Roeffaers, M. B. J.; Hofkens, J.; Wang, H. I.; Bonn, M. Highly Mobile Large Polarons in Black Phase CsPbI3. *Acs Energy Lett.* **2021**, *6* (2), 568−573.
(9) Beard, M. C.; Turner, G. M.; Norris, D. J.; Schmuttenmaer, C. A. Photoconductivity in CdSe nanoparticles studied by time-resolved terahertz spectroscopy (TRTS). *Abstr. Pap. Am. Chem. Soc.* **2000**, *219*, U582−U582.
(10) Doherty, T. A.; Winchester, A. J.; Macpherson, S.; Johnstone, D. N.; Pareek, V.; Tennyson, E. M.; Kosar, S.; Kosasih, F. U.; Anaya, M.; Abdi-Jalebi, M.; et al. Performance-limiting nanoscale trap clusters at grain junctions in halide perovskites. *Nature* **2020**, *580* (7803), 360−366.
(11) Li, C. B.; Wang, A. L.; Deng, X. Y.; Wang, S. R.; Yuan, Y.; Ding, L. M.; Hao, F. Insights into Ultrafast Carrier Dynamics in Perovskite Thin Films and Solar Cells. *Acs Photonics* **2020**, *7* (8), 1893−1907.
(12) Morimoto, T.; Nagai, M.; Minowa, Y.; Ashida, M.; Yokotani, Y.; Okuyama, Y.; Kani, Y. Microscopic ion migration in solid electrolytes revealed by terahertz time-domain spectroscopy. *Nat. Commun.* **2019**, *10* (1), 2662.
(13) Musiienko, A.; Pipek, J.; Praus, P.; Brynza, M.; Belas, E.; Dryzhakov, B.; Du, M. H.; Ahmadi, M.; Grill, R. Deciphering the effect of traps on electronic charge transport properties of methylammonium lead tribromide perovskite. *Sci. Adv.* **2020**, *6* (37), 1.
(14) Petrovic, M.; Ye, T.; Vijila, C.; Ramakrishna, S. Influence of Charge Transport and Defects on the Performance of Planar and Mesostructured Perovskite Solar Cells. *Adv. Energy Mater.* **2017**, *7* (13), 1602610.
(15) Clarke, T. M.; Lungenschmied, C.; Peet, J.; Drolet, N.; Mozer, A. J. A comparison of five experimental techniques to measure charge carrier lifetime in polymer/fullerene solar cells. *Adv. Energy Mater.* **2015**, *5* (4), 1401345.
(16) Adhikari, P.; Kobbekaduwa, K.; Shi, Y.; Zhang, J. B.; Al Abass, N.; He, J.; Rao, A.; Gao, J. B. Sub-50 ps to microsecond carrier transport dynamics in pentacene thin films. *Appl. Phys. Lett.* **2018**, *113* (18), 183509 DOI: 10.1063/1.5048108.
(17) Gao, J. B.; Rao, A. M.; Li, H. B.; Zhang, J. B.; Chen, O. Carrier Transport Dynamics in High Speed Black Phosphorus Photodetectors. *Acs Photonics* **2018**, *5* (4), 1412−1417.
(18) Kobbekaduwa, K.; Shrestha, S.; Adhikari, P.; Liu, E. X.; Coleman, L.; Zhang, J. B.; Shi, Y.; Zhou, Y. Y.; Bekenstein, Y.; Yan, F.; et al. In-situ observation of trapped carriers in organic metal halide perovskite films with ultra-fast temporal and ultra-high energetic resolutions. *Nat. Commun.* **2021**, *12* (1), 1636.
(19) Yi, H. T.; Wu, X.; Zhu, X.; Podzorov, V. Intrinsic charge transport across phase transitions in hybrid organo-inorganic perovskites. *Adv. Mater.* **2016**, *28* (30), 6509−6514.
(20) Moses, D. Mechanism of carrier photogeneration in amorphous selenium: Fast transient photoconductivity. *Phys. Rev. B* **1996**, *53* (8), 4462−4470.
(21) Szeremeta, J.; Antoniak, M. A.; Wawrzyńczyk, D.; Nyk, M.; Samoć, M. The two-photon absorption cross-section studies of CsPbX3 (X= I, Br, Cl) nanocrystals. *Nanomaterials* **2020**, *10* (6), 1054.
(22) Amith, A.; Kudman, I.; Steigmeier, E. Electron and phonon scattering in GaAs at high temperatures. *Phys. Rev.* **1965**, *138* (4A), A1270.
(23) Jacoboni, C.; Canali, C.; Ottaviani, G.; Quaranta, A. A. A review of some charge transport properties of silicon. *Solid-State Electron.* **1977**, *20* (2), 77−89.
(24) Li, B.; Zhang, Y.; Fu, L.; Yu, T.; Zhou, S.; Zhang, L.; Yin, L. Surface passivation engineering strategy to fully-inorganic cubic CsPbI3 perovskites for high-performance solar cells. *Nat. Commun.* **2018**, *9* (1), 1076.
(25) Jin, H. D.; Debroye, E.; Keshavarz, M.; Scheblykin, I. G.; Roeffaers, M. B. J.; Hofkens, J.; Steele, J. A. It's a trap! On the nature of localised states and charge trapping in lead halide perovskites. *Mater. Horiz* **2020**, *7* (2), 397−410.
(26) Knight, A. J.; Patel, J. B.; Snaith, H. J.; Johnston, M. B.; Herz, L. M. Trap States, Electric Fields, and Phase Segregation in Mixed-Halide Perovskite Photovoltaic Devices. *Adv. Energy Mater.* **2020**, *10* (9), 1903488.

(27) Giovanni, D.; Righetto, M.; Zhang, Q. N.; Lim, J. W. M.; Ramesh, S.; Sum, T. C. Origins of the long-range exciton diffusion in perovskite nanocrystal films: photon recycling vs exciton hopping. *Light-Sci. Appl.* **2021**, *10* (1), 2.
(28) Xing, G. C.; Mathews, N.; Sun, S. Y.; Lim, S. S.; Lam, Y. M.; Gratzel, M.; Mhaisalkar, S.; Sum, T. C. Long-Range Balanced Electron- and Hole-Transport Lengths in Organic-Inorganic CH3NH3PbI3. *Science* **2013**, *342* (6156), 344−347.
(29) Chan, C. C. S.; Fan, K. Z.; Wang, H.; Huang, Z. F.; Novko, D.; Yan, K. Y.; Xu, J. B.; Choy, W. C. H.; Loncaric, I.; Wong, K. S. Uncovering the Electron-Phonon Interplay and Dynamical Energy-Dissipation Mechanisms of Hot Carriers in Hybrid Lead Halide Perovskites. *Adv. Energy Mater.* **2021**, *11* (9), 2003071.
(30) Dresselhaus, M.; Dresselhaus, G.; Cronin, S. B.; Souza Filho, A. G. *Solid State Properties*. Springer-Verlag: Germany, 2018.
(31) Poncé, S.; Schlipf, M.; Giustino, F. Origin of low carrier mobilities in halide perovskites. *ACS Energy Letters* **2019**, *4* (2), 456−463.
(32) Milot, R. L.; Eperon, G. E.; Snaith, H. J.; Johnston, M. B.; Herz, L. M. Temperature-dependent charge-carrier dynamics in CH3NH3PbI3 perovskite thin films. *Adv. Funct. Mater.* **2015**, *25* (39), 6218−6227.
(33) Davies, C. L.; Borchert, J.; Xia, C. Q.; Milot, R. L.; Kraus, H.; Johnston, M. B.; Herz, L. M. Impact of the organic cation on the optoelectronic properties of formamidinium lead triiodide. *journal of physical chemistry letters* **2018**, *9* (16), 4502−4511.
(34) Schotz, K.; Askar, A. M.; Kohler, A.; Shankar, K.; Panzer, F. Investigating the Tetragonal-to-Orthorhombic Phase Transition of Methylammonium Lead Iodide Single Crystals by Detailed Photoluminescence Analysis. *Adv. Opt Mater.* **2020**, *8* (17), 2000455.
(35) Paulus, F.; Tyznik, C.; Jurchescu, O. D.; Vaynzof, Y. Switched-On: Progress, Challenges, and Opportunities in Metal Halide Perovskite Transistors. *Adv. Funct Mater.* **2021**, *31* (29), 2101029.
(36) Schilcher, M. J.; Robinson, P. J.; Abramovitch, D. J.; Tan, L. Z.; Rappe, A. M.; Reichman, D. R.; Egger, D. A. The significance of polarons and dynamic disorder in halide perovskites. *ACS Energy Letters* **2021**, *6* (6), 2162−2173.
(37) Motta, C.; Sanvito, S. Electron−phonon coupling and polaron mobility in hybrid perovskites from first principles. *J. Phys. Chem. C* **2018**, *122* (2), 1361−1366.
(38) Frost, J. M. Calculating polaron mobility in halide perovskites. *Phys. Rev. B* **2017**, *96* (19), 195202.
(39) Lee, J. H.; Lee, J.-H.; Kong, E.-H.; Jang, H. M. The nature of hydrogen-bonding interaction in the prototypic hybrid halide perovskite, tetragonal CH3NH3PbI3. *Sci. Rep.* **2016**, *6* (1), 1−12.
(40) Kennehan, E. R.; Doucette, G. S.; Marshall, A. R.; Grieco, C.; Munson, K. T.; Beard, M. C.; Asbury, J. B. Electron−Phonon Coupling and Resonant Relaxation from 1D and 1P States in PbS Quantum Dots. *ACS Nano* **2018**, *12* (6), 6263−6272.
(41) Fivaz, R.; Mooser, E. Mobility of charge carriers in semiconducting layer structures. *Phys. Rev.* **1967**, *163* (3), 743.
(42) Mirlin, D. N.; Karlik, I. J.; Nikitin, L. P.; Reshina, I. I.; Sapega, V. F. Hot electron photoluminescence in GaAs crystals. *Solid State Commun.* **1981**, *37* (9), 757−760.
(43) Hinckley, J. M.; Singh, J. Monte Carlo studies of ohmic hole mobility in silicon and germanium: Examination of the optical phonon deformation potential. *Journal of applied physics* **1994**, *76* (7), 4192−4200.
(44) Saran, R.; Heuer-Jungemann, A.; Kanaras, A. G.; Curry, R. J. Giant bandgap renormalization and exciton−phonon scattering in perovskite nanocrystals. *Advanced Optical Materials* **2017**, *5* (17), 1700231.
(45) Kaczkowski, J.; Płowaś-Korus, I. The Vibrational and Thermodynamic Properties of CsPbI3 Polymorphs: An Improved Description Based on the SCAN meta-GGA Functional. *journal of physical chemistry letters* **2021**, *12* (28), 6613−6621.
(46) Marronnier, A.; Lee, H.; Geffroy, B.; Even, J.; Bonnassieux, Y.; Roma, G. Structural instabilities related to highly anharmonic phonons in halide perovskites. *journal of physical chemistry letters* **2017**, *8* (12), 2659−2665.

https://doi.org/10.1021/acsnano.3c03989
ACS Nano 2023, 17, 13997−14004